Construction and Building Materials 394 (2023) 132211

Contents lists available at ScienceDirect

Construction and Building Materials

journal homepage: www.elsevier.com/locate/conbuildmat

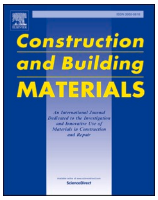

Modelling of 3D periodic cathodic protection problems in reinforced concrete structures with accelerated boundary element method

Dimitrios T. Kalovelonis [a], Theodoros V. Gortsas [b,a], Stephanos V. Tsinopoulos [b,*]

[a] Department of Mechanical Engineering & Aeronautics, University of Patras, Greece
[b] Department of Mechanical Engineering, University of Peloponnese, Greece

ARTICLE INFO

Keywords:
Reinforced Concrete Corrosion
Cathodic Protection
BEM
ACA/ BEM
Macrocell corrosion

ABSTRACT

The steel used for concrete reinforcement exhibits either active or passive electrochemical behavior. As long as the concrete environment remains highly alkaline, the steel remains passive. However, carbonation and/or chloride contamination of concrete will cause steel to become active and corrode. In the latter case, a common strategy is the use of cathodic protection (CP) systems to lower the potential of the steel at a protective level. The numerical modelling of cathodically protected concrete buildings and infrastructures usually requires large-scale models due to their size and complex geometry. An efficient modelling approach is to consider any possible periodicity in these problems by applying periodic boundary conditions to a representative volume element of the structure. The boundary element method (BEM) is extensively used for solving CP problems. A BEM formulation is proposed for solving 3D periodic CP problems in this work. The computation cost is reduced by applying acceleration techniques based on adaptive cross approximation (ACA). As an engineering application, a sacrificial anode CP system of a reinforced concrete column is designed, illustrating the importance of detailed modelling in the design of such systems. To this end, the macrocell corrosion problem is initially solved, and a parametric study with respect to concrete conductivity is carried out.

1. Introduction

Steel bars are placed in concrete to achieve the required tensile strength. Steel, used for concrete reinforcement, exhibits either active or passive electrochemical behavior. As long as the concrete environment remains highly alkaline, steel remains passive [1–3]. A thin passive oxide film forms on the reinforcing steel, which is only maintained at high pH values (~14) [3]. However, the ordinarily passive steel may corrode due to carbonation and/or chloride-induced corrosion [1–3]. Due to its porous nature, concrete is contaminated with atmospheric carbon dioxide and chloride ions. During carbonation, the pH decreases from ~14 to ~8 due to the formation of carbonic acid. At this pH, corrosion of the reinforcement is activated, leading to the formation of porous rust [1,2]. In a concrete column, due to carbonation and/or chloride contamination, a part of the steel reinforcement becomes active while the rest remains passive [1,2]. Due to the potential difference between active and passive steel parts, macrocell corrosion occurs, and the active steel becomes anodic while the passive becomes cathodic [4]. Cases of carbonated concrete containing high chloride levels simultaneously can be found, for instance, inside road tunnels [5].

Another reinforcement corrosion type is chloride-induced damage. Chloride movement through concrete is due to diffusion [6,7]. Chloride ions act as an iron dissolution catalyst and may destroy the passive ferric oxide film even at high alkalinities and very low concentrations [1,8], resulting in pitting corrosion. Another corrosion type of steel concrete reinforcement is alternating current corrosion, where the presence of a high alternating electric field causes the breakdown of the passive film [9,10], resulting in localized corrosion of passive steel [11,12].

Several methods can be used for corrosion control of reinforcement steel, such as using inhibitors in the concrete [1,13,14,15], applying coatings on the concrete (zinc or organic) and/or on the steel [1,13,15], removing the chloride ions [1] and installing cathodic protection (CP) systems [1,13,15]. Regulations and standards [16,17] recommend that in the case of active reinforcement corrosion, steel potential should be lowered through CP. Generally, the performance of a CP system is affected by several parameters, such as the concrete conductivity, the chloride and oxygen content in the concrete, the chemical composition of steel, and the carbonation depth [16,17,18].

The boundary element method (BEM) is a well-established numerical tool for solving CP problems. BEM offers the advantages of high solution

---

* Corresponding author.
E-mail address: stsinop@uop.gr (S.V. Tsinopoulos).

https://doi.org/10.1016/j.conbuildmat.2023.132211
Received 2 June 2022; Received in revised form 13 January 2023; Accepted 17 June 2023

accuracy, especially in the computation of potential gradients (current density), as well as reducing the problem dimensionality by one. The latter advantage is very pronounced, especially for infinite and semi-infinite electrolytes, since only the boundary surfaces must be discretized. The use of BEM for cathodic protection problems dates to 1982 when Fu & Chow [19] modelled an axisymmetric electrochemical tank. Since then, BEM has been extensively used for solving CP problems dealing with marine applications (e.g. [20–27]), underground structures (e.g. [28,29],), and concrete reinforcement (e.g. [30–36]). Furthermore, using BEM, Brichau et.al [37], Treveleyan and Hack [38], Adey and Baynham [39], and Kalovelonis et. al [40], solved stray current corrosion problems, Deconinck et.al. [41] modelled the electrode shape change, and DeGiorgi [42], Brichau and Deconinck [43] and Riemer and Orazem [44] modelled the coating breakdown and flaws using BEM. Also, BEM has been used to solve CP design optimization problems (e.g. [45–49]). The above-mentioned models are either two or three dimensional. Also, axisymmetric BEM formulations [50] and line elements [51] have been introduced to reduce the calculations. In the last decades, the BEM has become much more attractive to use by overcoming the disadvantages of time-consuming computations and the high demand for computer memory, utilizing acceleration techniques such as fast multipole [52,53] and adaptive cross approximation (ACA) [25–27,40]. With these techniques, it is possible to efficiently solve large-scale CP engineering problems with million degrees of freedom in a standard workstation [25–27,40].

The numerical modelling of cathodically protected concrete buildings and infrastructures usually requires large-scale models due to their size and complex geometry. In the literature, real-world reinforced concrete CP problems are usually solved using 2D [54,55] or simplified 3D models [30–32,50], where a small part of the concrete column is analyzed by applying insulation boundary conditions on the outer column surfaces. An efficient modelling approach is to consider the periodicity appearing in these problems. To this end, a representative volume of the structure is considered, and periodic boundary conditions are applied [56]. To the best of our knowledge, a BEM formulation for solving CP problems, considering the existing periodicity, has not yet been proposed in the literature.

The goal of the present work is twofold. First, a BEM formulation for solving periodic 3D CP problems is proposed, implementing periodic boundary conditions for the first time. To accelerate the computations of the proposed BEM, the ACA/BEM presented in [27] is extended appropriately so that large-scale CP problems can be solved efficiently in a standard workstation. Second, a large-scale problem of a sacrificial anode CP system to protect the steel reinforcement of an infinitely extended periodic concrete column is solved. Due to carbonation and chloride contamination, a part of the steel reinforcement is considered active, while the rest remains passive. Because of the potential difference between active and passive steel, the macrocell corrosion problem is initially solved to assess the CP system design. Finally, a parametric study with respect to concrete conductivity is carried out to evaluate the performance of the CP system. The problems are solved utilizing a highly detailed model for the geometry of the real-world structure.

The paper is organized as follows. Sections 2 and 3 describe the mathematical modelling of periodic CP problems and the proposed BEM formulation. In Section 4, the numerical verification of the proposed method and its application to the above-mentioned CP problem are presented. Finally, the main conclusions drawn from the present work are provided in Section 5.

2. Mathematical modelling of CP systems with periodic structure

In dilute solutions, the transport of species is governed by the Nernst-Planck equation. In stationary and electroneutral solutions, assuming that the homogenous reactions are electrically balanced, the Nernst-Planck equation reduces to charge conservation [57].

$$\nabla\cdot\mathbf{i} = 0 \tag{1}$$

where $\mathbf{i}$ is the current density vector. Without concentration variations in the electrolyte, the current density is proportional to the potential gradient [57].

$$\mathbf{i} = -\sigma\nabla\varphi \tag{2}$$

where σ is the electrical conductivity and φ is the electric potential. Assuming that the electrical conductivity is constant everywhere in the electrolyte, Eq. (1) yields to Laplace Equation

$$\nabla^2\varphi = 0 \tag{3}$$

The projection of current density vector $\mathbf{i}$, at a surface point with a unit normal vector $\widehat{\mathbf{n}}$ is defined as follows:

$$i = \widehat{\mathbf{n}}\cdot\mathbf{i} = -\sigma\,\widehat{\mathbf{n}}\cdot\nabla\varphi = -\sigma\,\partial_n\varphi \tag{4}$$

where $\widehat{\mathbf{n}}$ is the unit normal vector, and $\partial_n\varphi = \widehat{\mathbf{n}}\cdot\nabla\varphi$, is the normal derivative of the electric potential at the surface of the electrolyte (potential flux).

Consider a periodic 3D structure infinitely extended in one of the three dimensions, exhibiting linear periodicity, as shown in Fig. 1. The structure is protected by a CP system, with its anodes also arranged periodically. The modelling of the above-described CP problem can be significantly simplified considering a representative volume element (RVE), as shown in Fig. 1. The RVE is enclosed by the fictitious periodic interface boundaries S_{f_1} and S_{f_2}, and the physical boundary $S_p = S_q \cup S_c \cup S_a$, with S_q being the outer boundary and S_c and S_a, the interior boundaries corresponding to the steel and the anode surfaces. The expected symmetric pattern behavior of the unknown potential and current density is imposed by applying the appropriate periodic conditions to the fictitious boundaries S_{f_1} and S_{f_2}.

On the physical boundary $S_p = S_c \cup S_a \cup S_q$ of the RVE, the following boundary conditions are applied:

$$i(\mathbf{x}) = f(\varphi(\mathbf{x})),\quad \mathbf{x}\in\ S_c \tag{5}$$

$$\left.\begin{array}{ll} \varphi(\mathbf{x}) = \varphi_0 & \text{(i)} \\ \text{or} & \\ i(\mathbf{x}) = g(\varphi(\mathbf{x})) & \text{(ii)} \end{array}\right\},\quad \mathbf{x}\in S_a \quad \text{for sacrificial anodes} \tag{6}$$

$$i(\mathbf{x}) = i_{app},\quad \mathbf{x}\in S_a \quad \text{for impressed anodes} \tag{7}$$

$$i(\mathbf{x}) = 0,\quad \mathbf{x}\in S_q \tag{8}$$

At the cathode and anode surfaces, non-linear polarization curves can be assigned (Eq. (5) and Eq. (6.ii)), which describes the activation and/or concentration polarization of the metal-electrolyte interface [25–27,40,57]. At the anode, when the polarization can be neglected,

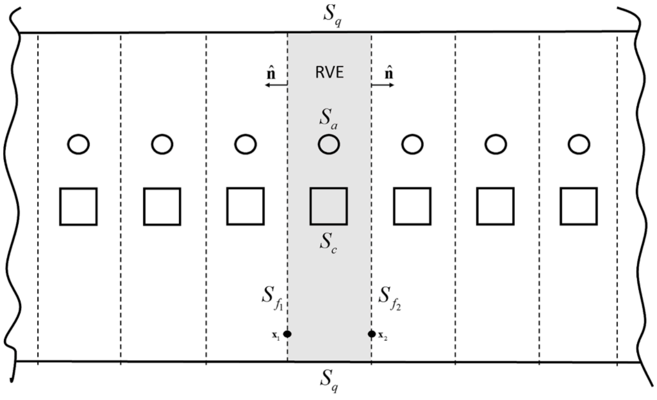

Fig. 1. Schematic representation of a CP system with periodic structure.

constant potential (equal to the metal's equilibrium potential) can be assigned (Eq. (6.i)) [57]. On the impressed anode surfaces, constant values of current density are imposed (Eq. (7)) [25–27,40]. At last, on the bounding box surfaces, zero current density condition is assigned (Eq. (8)) [25–27,40].

At the fictitious periodic boundaries S_{f_1} and S_{f_2}, the following conditions are applied:

$$\varphi(\mathbf{x}_1) = \varphi(\mathbf{x}_2) \tag{9}$$

$$i(\mathbf{x}_1) = -i(\mathbf{x}_2) \tag{10}$$

where $\mathbf{x}_1 \in S_{f_1}$ and $\mathbf{x}_2 \in S_{f_2}$ (Fig. 1), with $\mathbf{x}_2 = \mathbf{x}_1 + \mathbf{t}$ where $\mathbf{t}$ is a constant translation vector at the direction of the periodicity, that translates S_{f_1} to S_{f_2}.

3. BEM formulation for periodic CP systems

The well-posed boundary value problem, which consists of Eq. (3), the boundary conditions (5)-(8) and the periodic conditions (9)-(10), is solved numerically by the BEM. The integral form of Eq. (3) reads [58]:

$$c(\mathbf{x})\varphi(\mathbf{x}) + \int_S \partial_n G(\mathbf{x},\mathbf{y})\varphi(\mathbf{y})dS_y = \int_S G(\mathbf{x},\mathbf{y})\partial_n\varphi(\mathbf{y})dS_y \tag{11}$$

where $S = S_p \cup S_{f_1} \cup S_{f_2}$, $c(\mathbf{x})$ is a coefficient that depends on the local smoothness of the surface, $\mathbf{x}$ and $\mathbf{y}$ are points that lie on the surface S, $G(\mathbf{x},\mathbf{y})$ is the full space fundamental solution of the Laplace equation, and $\partial_n G(\mathbf{x},\mathbf{y})$ is its normal derivative given in three dimensions by the following expressions [58]:

$$\begin{aligned} G(\mathbf{x},\mathbf{y}) &= \frac{1}{4\pi|\mathbf{r}|} \\ \partial_n G(\mathbf{x},\mathbf{y}) &= -\frac{1}{4\pi|\mathbf{r}|^3}\mathbf{r}\cdot\widehat{\mathbf{n}} \\ \mathbf{r} &= \mathbf{y} - \mathbf{x} \end{aligned} \tag{12}$$

The boundaries S are discretized into quadrilateral or/and triangular surface elements. In each element, the fields $\varphi(\mathbf{x})$ and $\partial_n\varphi(\mathbf{x})$ are assumed to be constant. Then, the boundary integral equation (11), written for the collocation point located at the center of the element i, obtains the following discrete form

$$\frac{1}{2}\varphi^i + \sum_{e=1}^{E} H_{ie}\varphi^e = \sum_{e=1}^{E} G_{ie}q^e \tag{13}$$

where E denote the total number of elements, the symbol q indicates potential flux ($q = \partial_n\varphi$), while the integrals H and G have the form

$$H_{ie} = \int_{-1}^{1}\int_{-1}^{1} \partial_n G\left(\mathbf{x}^i, \mathbf{y}^e(\xi_1,\xi_2)\right)|\mathbf{J}^e|d\xi_1 d\xi_2 \tag{14}$$

$$G_{ie} = \int_{-1}^{1}\int_{-1}^{1} G\left(\mathbf{x}^i, \mathbf{y}^e(\xi_1,\xi_2)\right)|\mathbf{J}^e|d\xi_1 d\xi_2 \tag{15}$$

where $\mathbf{J}^{\mathrm{e}}$ stands for the Jacobian matrix of the transformation from the global Cartesian to the local coordinate system. The integrals of Eqs. (14) and (15) are evaluated numerically via highly accurate, direct integration techniques illustrated in [59].

Collocating Eq. (13) at all collocation points, the following linear system of equations is obtained:

$$\begin{aligned} &\begin{bmatrix} \overline{\mathbf{H}}^{(S_pS_p)} & \mathbf{H}^{(S_pS_{f_1})} & \mathbf{H}^{(S_pS_{f_2})} \\ \mathbf{H}^{(S_{f_1}S_p)} & \overline{\mathbf{H}}^{(S_{f_1}S_{f_1})} & \mathbf{H}^{(S_{f_1}S_{f_2})} \\ \mathbf{H}^{(S_{f_2}S_p)} & \mathbf{H}^{(S_{f_2}S_{f_1})} & \overline{\mathbf{H}}^{(S_{f_2}S_{f_2})} \end{bmatrix} \cdot \begin{Bmatrix} \boldsymbol{\varphi}^{(S_p)} \\ \boldsymbol{\varphi}^{(S_{f_1})} \\ \boldsymbol{\varphi}^{(S_{f_2})} \end{Bmatrix} = \\ &\begin{bmatrix} \mathbf{G}^{(S_pS_p)} & \mathbf{G}^{(S_pS_{f_1})} & \mathbf{G}^{(S_pS_{f_2})} \\ \mathbf{G}^{(S_{f_1}S_p)} & \mathbf{G}^{(S_{f_1}S_{f_1})} & \mathbf{G}^{(S_{f_1}S_{f_2})} \\ \mathbf{G}^{(S_{f_2}S_p)} & \mathbf{G}^{(S_{f_2}S_{f_1})} & \mathbf{G}^{(S_{f_2}S_{f_2})} \end{bmatrix} \cdot \begin{Bmatrix} \mathbf{q}^{(S_p)} \\ \mathbf{q}^{(S_{f_1})} \\ \mathbf{q}^{(S_{f_2})} \end{Bmatrix} \end{aligned} \tag{16}$$

with $[\overline{\mathbf{H}}] = \left[\frac{1}{2}\mathbf{I} + \mathbf{H}\right]$. In the characterization (S_iS_j) of each matrix block appearing in Eq. (16), the first symbol indicates the surface where the collocation points are located, while the second symbol indicates the surface of the boundary elements, for which the integrals of Eqs. (14) and (15) are computed. To apply the periodic conditions (9) and (10), the linear system of Eq. (16) can be partitioned as:

$$\begin{aligned} &\begin{bmatrix} \overline{\mathbf{H}}^{(S_pS_p)} & \mathbf{H}^{(S_pS_{f_1})} + \mathbf{H}^{(S_pS_{f_2})} \\ \mathbf{H}^{(S_{f_1}S_p)} & \overline{\mathbf{H}}^{(S_{f_1}S_{f_1})} + \mathbf{H}^{(S_{f_1}S_{f_2})} \\ \mathbf{H}^{(S_{f_2}S_p)} & \mathbf{H}^{(S_{f_2}S_{f_1})} + \overline{\mathbf{H}}^{(S_2S_{f_2})} \end{bmatrix} \cdot \begin{Bmatrix} \boldsymbol{\varphi}^{(S_p)} \\ \boldsymbol{\varphi}^{(S_{f_1})} \end{Bmatrix} = \\ &\begin{bmatrix} \mathbf{G}^{(S_pS_p)} & \mathbf{G}^{(S_pS_{f_1})} - \mathbf{G}^{(S_pS_{f_2})} \\ \mathbf{G}^{(S_{f_1}S_p)} & \mathbf{G}^{(S_{f_1}S_{f_1})} - \mathbf{G}^{(S_{f_1}S_{f_2})} \\ \mathbf{G}^{(S_{f_2}S_p)} & \mathbf{G}^{(S_{f_2}S_{f_1})} - \mathbf{G}^{(S_{f_2}S_{f_2})} \end{bmatrix} \cdot \begin{Bmatrix} \mathbf{q}^{(S_p)} \\ \mathbf{q}^{(S_{f1})} \end{Bmatrix} \end{aligned} \tag{17}$$

Boundary conditions (5) and (6.ii) (polarization curves) correlate the potential with the current density in a non-linear way. For the solution of the system of algebraic eq. (17), an iterative Newton-Raphson procedure is applied. According to the Newton-Raphson scheme, Eq. (5) becomes

$$\partial_n\varphi^k(\mathbf{x}) = -\frac{1}{\sigma}f\left(\varphi^{k-1}(\mathbf{x})\right) - \frac{1}{\sigma}\frac{\partial f\left(\varphi^{k-1}(\mathbf{x})\right)}{\partial\varphi}\Delta\varphi^k(\mathbf{x}) \tag{18}$$

$$\varphi^k(\mathbf{x}) = \varphi^{k-1}(\mathbf{x}) + \Delta\varphi^k(\mathbf{x}) \tag{19}$$

where the index k represents the Newton-Raphson iteration step. Similar equations are obtained for the polarization curve of Eq. (6.ii)). Rearranging Eq. (17) with the aid of Eqs. (18) and (19), the linear boundary conditions of Eqs. (6.i), (7) and (8), the following linear algebraic system of equations, is produced, for each iteration k

$$\left[\mathbf{A}^{k-1}\right]\cdot\left\{\mathbf{X}^k\right\} = \left\{\mathbf{B}^{k-1}\right\} \tag{20}$$

Finally, the linear algebraic system of Eq. (20) is solved, for each iteration k, by means of the iterative GMRES solver with a chosen accuracy $\varepsilon_{\mathrm{GMR}}$. The iterative solution is accelerated by a hierarchical LU preconditioner with a chosen accuracy $\varepsilon_{\mathrm{LU}}$ [25,27].

4. Numerical results

The goal of the present section is twofold. In a first step, to verify that the proposed ACA/BEM formulation for periodic CP problems works properly, a benchmark problem is solved. Then, a problem concerning a three-dimensional periodic concrete rebar, which exhibits both active and passive electrochemical behavior, protected by a CP system, is studied.

4.1. Benchmark problem

Consider an infinitely extended at z-direction concrete prismatic block, with a square cross-section of side 400 mm, reinforced by a rebar of diameter 100 mm, as shown in Fig. 2. The rebar is cathodically protected by sacrificial zinc anodes. The anodes are rectangular blocks of length 100 mm and cross-section of 50 × 15 mm, and they are placed with their length parallel to the main axis of the rebar, in a periodic distribution. The distance between two consecutive anodes is 800 mm, and the minimum distance between the rebar and the anodes is 69.5

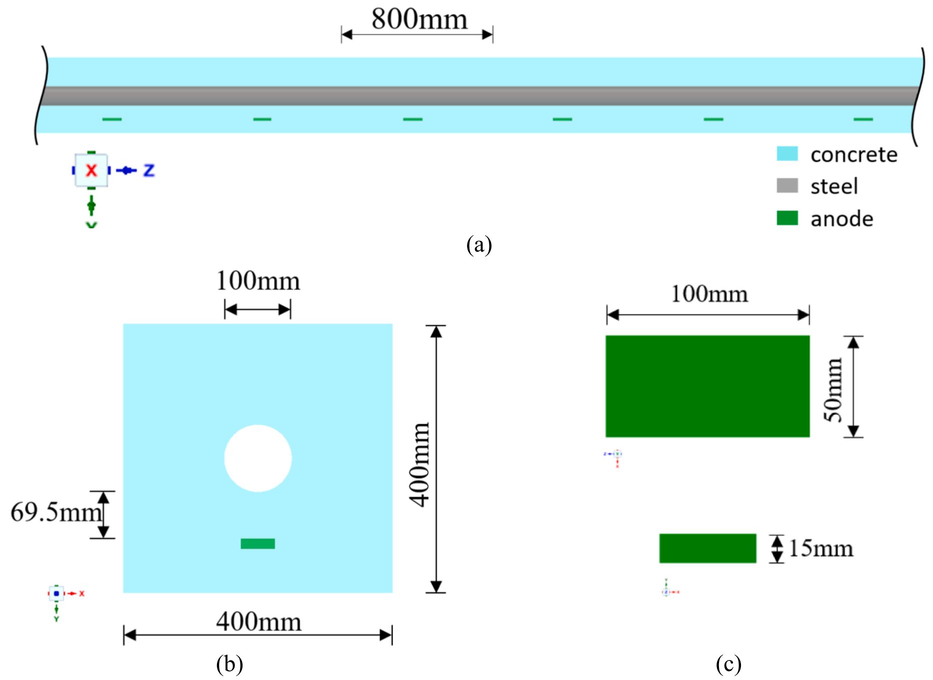

Fig. 2. (a) The infinitely extended concrete block; (b) Cross-section geometry and (c) Sacrificial anode.

mm.

The problem is solved via the proposed ACA/BEM formulation considering an RVE as shown in Fig. 3. The chosen RVE is the smallest possible one to generate the periodic geometry of the structure, having length 800 mm, and containing a single anode.

For concrete, an electrical conductivity $\sigma = 0.012$ S/m [60] is adopted. It is assumed that the steel polarization is governed by the following equation [56]:

$$i = i_{corr}\left\{ e^{\left[\frac{2.303(\varphi - E_{corr})}{b_a}\right]} - e^{\left[\frac{-2.303(\varphi - E_{corr})}{b_c}\right]} \right\} \tag{21}$$

where $i_{corr} = 1.0 \times 10^{-4}\mathrm{A/m^2}$, $E_{corr} = -0.1$ V vs SCE, $b_a = 1.0$ V/dec and $b_c = 0.2$ V/dec [18,61,62,63]. At the surface of the anode, a constant potential of $\varphi = -1.01$ V vs SCE [64] has been applied. The left and right-side boundaries of the RVE are modelled as periodic interfaces, while at rest concrete surfaces, insulating boundary conditions are applied, as shown in Fig. 3.

For validation purposes the problem is solved utilizing Siemens Simcenter STAR-CCM+ [56]. The potential distribution on the surface of the rebar, obtained by the proposed ACA/BEM and Siemens Simcenter

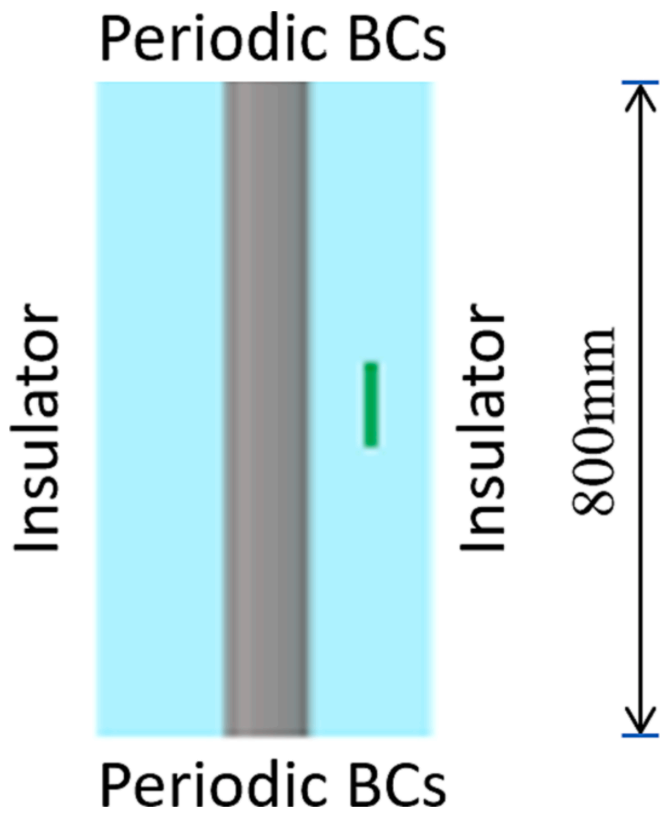

Fig. 3. Description of the RVE.

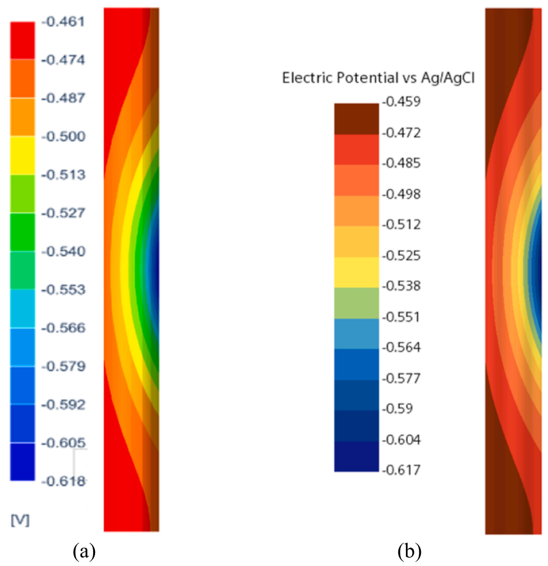

Fig. 4. Potential distribution on the steel surface with (a) the proposed formulation (b) Simcenter STAR CCM+.

STAR-CCM+, is illustrated in Fig. 4(a) and 4(b), respectively. Similarly, the current density distribution is plotted in Fig. 5(a) and 5(b). As it is evident, the obtained results are in excellent agreement verifying that the proposed ACA/BEM solves accurately periodic CP problems.

4.2. Analysis of reinforced concrete column protected by sacrificial anodes

This section presents the analysis of a reinforced concrete column exhibiting both active and passive behavior due to carbonation and chloride contamination, using a detailed model and the proposed ACA/BEM formulation. Due to the potential difference between active and passive steel, macrocell corrosion occurs, where the active steel becomes anodic and the passive cathodic. Initially, the macrocell corrosion is studied to be used as a reference solution. Then, the performance of the applied sacrificial anode cathodic protection (SACP) system is examined.

4.2.1. Geometry and CP system configuration

Consider a long periodic reinforced concrete column with a square cross-section of 400 mm × 400 mm, as shown in Fig. 6(a). The horizontal and vertical bars in the rebar frame are of diameter 8 mm and 14 mm, respectively. The length of a cell of the rebar grid is 200 mm, and the total area of the steel surface in each cell is 74930 mm^2. A SACP system protects the rebar with the zinc anodes placed periodically, forming the repeating pattern shown in Fig. 6(b). The anodes are plates of dimensions 50 mm × 50 mm × 20 mm, placed in the middle of the cell of the rebar grid, as shown in Fig. 6(b) and 6(c). The minimum distance between the anodes and the concrete block is 10 mm.

The repeating pattern in Fig. 6(b), containing three consecutive anodes, is chosen as the RVE of the problem. Note that, with the present design of the CP system, a certain number of cells of the rebar grid do not contain any anode. The length of the RVE is 800 mm, noting that the total area of the steel surface in the RVE is 299720 mm^2.

4.2.2. Electrochemical properties

In the present study, active corrosion of the rebar is considered due to carbonation and chloride contamination. The carbonation depth is modelled as a function of the square root of time [65]. Considering that the structure was constructed 40 years ago and adopting a value K = 6 (mm.yr$^{-1/2}$) for the carbonation rate constant [65], a resulting carbonation depth of 38 mm is computed. The rebar steel located in the carbonated region is active, while the rest remains passive, as shown in Fig. 7(a), noting that the total area of the active and passive steel is 113038 mm^2 and 186682 mm^2, respectively.

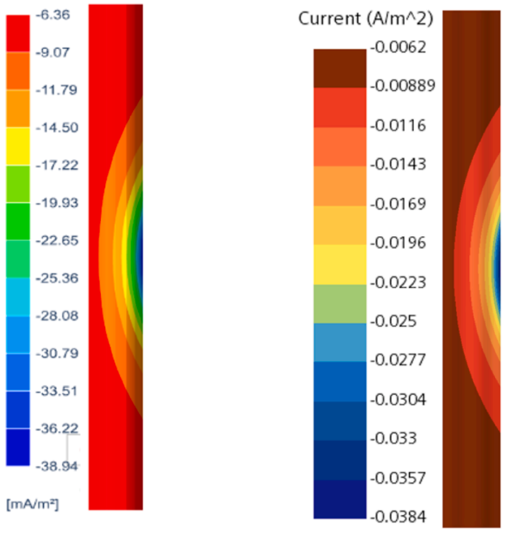

(a) (b)

Fig. 5. Current density distribution on the steel surface with (a) the proposed formulation (b) Simcenter STAR CCM+.

The cathodic part of active and passive steel polarization curves in concrete, as given in [18], are depicted in Fig. 7(b). Due to the potential difference between the active and passive steel surfaces, macrocell corrosion occurs, where the active steel functions as an anode, while the passive one becomes a cathode. Consequently, the anodic part of the active steel polarization curve is needed to model macrocell corrosion. Since only the cathodic part is available in Pedeferi [18], the anodic part $i_a(\varphi)$ is extracted from the cathodic one as follows:

Electrochemical corrosion of steel rebar occurs with the presence of oxygen [1]:

$$\textit{Anodic partial reaction}: Fe \rightarrow Fe^{2+} + 2e^{-} \tag{22}$$

$$\textit{Cathodic partial reaction}: O_2 + 2H_2O + 4e^{-} \rightarrow 4OH^{-} \tag{23}$$

The polarization curve $i(\varphi)$ is the summation of the partial anodic $i_a(\varphi)$ and cathodic $i_c(\varphi)$ reaction rates of Eqs (22) and (23), respectively. Furthermore, observing the curve of the active steel cathodic part in Fig. 7b, only activation polarization has been considered [1,57], i.e.:

$$i(\varphi) = i_a(\varphi) - i_c(\varphi) \tag{24}$$

$$i_a(\varphi) = i_{Fe}^0 e^{\frac{\varphi - E_{eq,Fe}}{B_{Fe}}} \tag{25}$$

$$i_c(\varphi) = i_{O_2}^0 e^{\frac{\varphi - E_{eq,O_2}}{B_{O_2}}} \tag{26}$$

where i_{Fe}^0 and $i_{O_2}^0$ are the iron dissolution and oxygen reduction exchange current densities, respectively,$E_{eq,Fe}$ and E_{eq,O_2} are the iron and oxygen equilibrium potentials while B_{Fe} and B_{O_2} are the iron dissolution and oxygen reduction Tafel slopes.

The unknown parameters i_{Fe}^0, $i_{O_2}^0$, B_{Fe}, B_{O_2},E_{eq,O_2} and $E_{eq,Fe}$ are calculated by fitting Eq. (24) to the active steel polarization curve of Fig. 7(b). In Eq. (24), $i_c(\varphi)$ is dominant ($i_c >> i_a$) when $\varphi < E_{corr}$ - φ_c, $i_a(\varphi)$ is dominant ($i_a >> i_c$) when $\varphi > E_{corr} + \varphi_a$ and both contributions of $i_c(\varphi)$ and $i_a(\varphi)$ are significant for $\varphi \in [E_{corr}$ - φ_c, $E_{corr} + \varphi_a$,].

Consequently, by adopting $\varphi_c = 0.15$ V vs SCE [66], the active steel curve of Fig. 7(b) is divided into two parts; a purely cathodic for $\varphi < E_{corr}$ - φ_c and a mixed one for $\varphi \in [E_{corr}$ - φ_c, $E_{corr}]$. Fitting Eq. (26) to the purely cathodic part, one obtains$i_{O_2}^0 = 8.6$ x10^{-7} A/m^2,$B_{O_2} = -0.126$ V and$E_{eq,O_2} = 0.511$ V vs SCE. Since the parameters $i_{O_2}^0$, B_{O_2}, and E_{eq,O_2} have been determined, fitting Eq. (24) to the mixed part, one obtains$i_{Fe}^0 =$ 5.0x10^{-8} A/m^2, $B_{Fe} = 0.05$ V and $E_{eq,Fe} = -0.85$ V vs SCE [1]. The computed anodic part of the active steel polarization curve is shown in Fig. 7(b). The calculated values of the polarization properties are summarized in Table 1, noting that they agree with the ones found in the literature [61–63,67,68].

At the surface of the zinc anodes, a constant potential of $\phi = -1.01$ V vs SCE [64] has been applied.

The concrete conductivity typically ranges from $\sigma = 0.0005$ to 0.02 S/m [60]. For the analyses of Sections 4.2.5 and 4.2.6, the value of $\sigma =$ 0.01 S/m has been adopted. In Section 4.2.7, a parametric study where concrete conductivity takes values in the above range is presented.

4.2.3. Corrosion protection criteria

According to NACE [16], if the corrosion potential E_{corr} of the steel in the concrete is less negative than − 200 mV vs SCE, then the steel is passivated, and no polarization is required for its protection. However, for E_{corr} more negative than − 200 mV vs SCE, where the steel is active, at least a value of 100 mV cathodic polarization should be achieved at the most anodic location using CP.

On the other hand, ISO [17] recommends the usage of CP for the corrosion protection of active steel, with the delivered current density

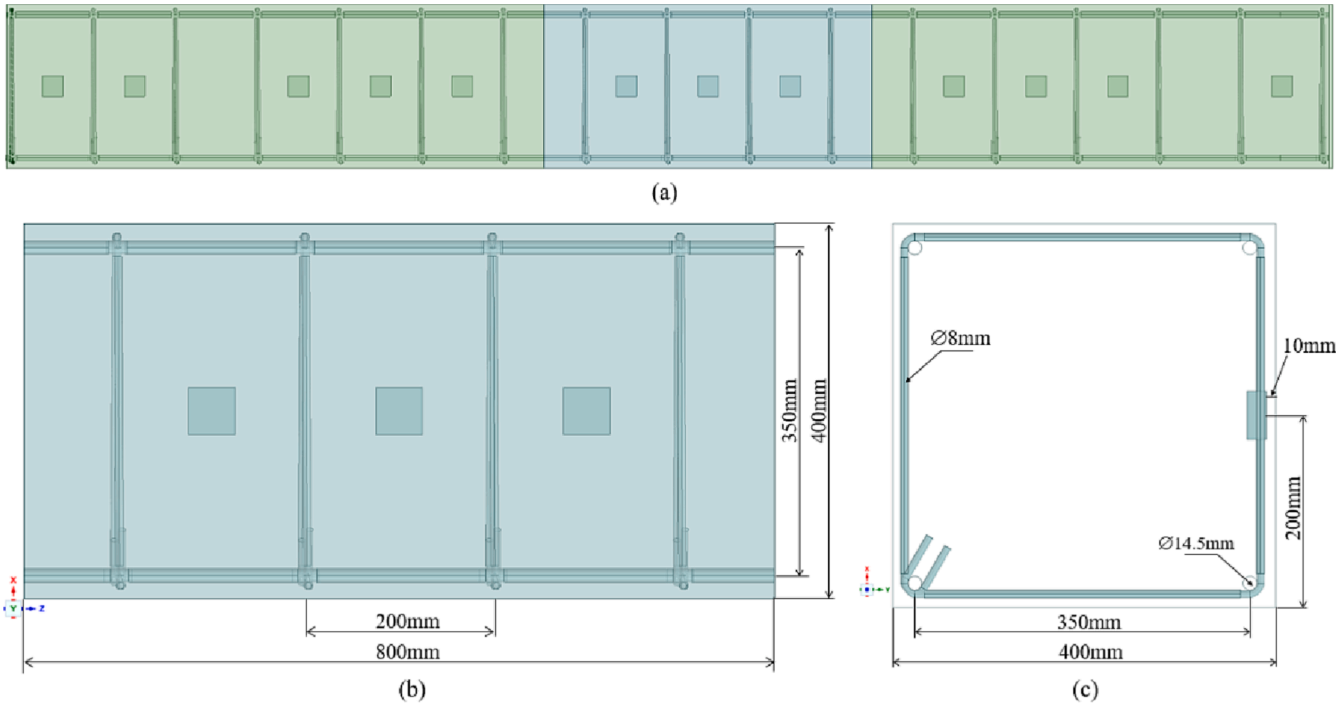

Fig. 6. (a) Long periodic reinforced concrete column protected by a SACP system; (b) Analyzed RVE; (c) Cross-section of the RVE.

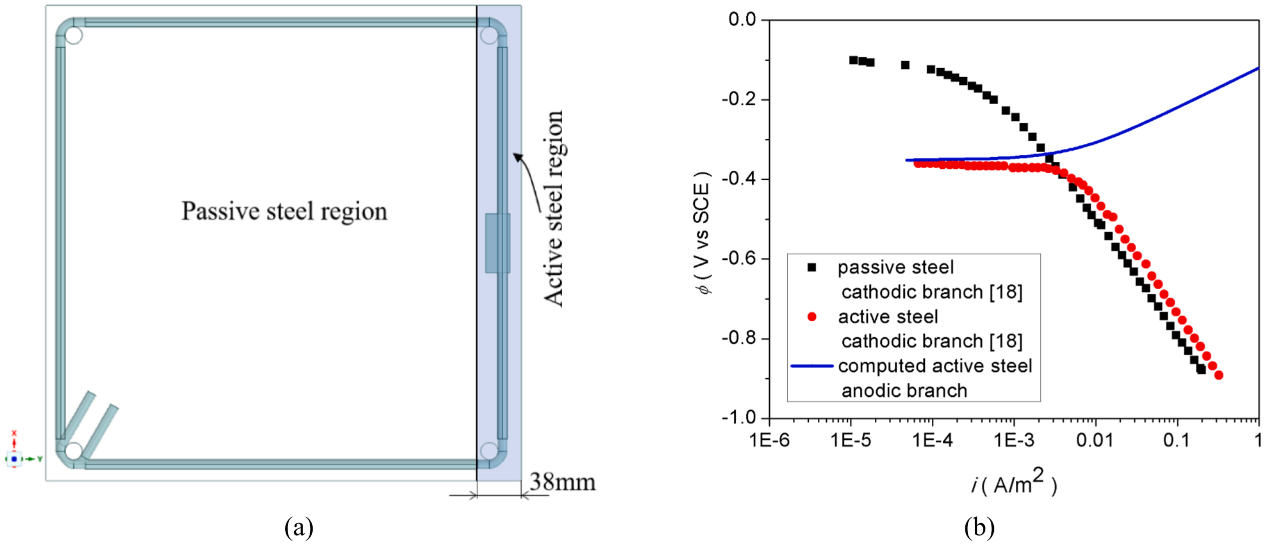

Fig. 7. (a) Active and passive steel regions of the model; (b) Polarization curves of active and passive steel.

Table 1
Active steel polarization curve properties.

Parameter	Calculated/Adopted values	Literature values ([61–63,67,68])
B_{Fe}	0.05 V	[0.03, 0.09] V
B_{O_2}	−0.126 V	[−0.23, − 0.12] V
i^0_{Fe}	5.0x10^{-8} A/m^2	[10^{-8}, 2.75x10^{-4}] A/m^2
$i^0_{O_2}$	8.6 x10^{-7} A/m^2	[6x10^{-8}, 1.2x10^{-6}] A/m^2
$E_{eq,Fe}$	−0.85 V vs SCE	[−0.906, −0,78] V vs SCE
E_{eq,O_2}	0.511 V vs SCE	[0.16, 0.541] V vs SCE

being in the range of 2–20 mA/m^2. Furthermore, for the prevention of passive steel, the delivered current density is recommended to be in the range of 0.2–2 mA/m^2.

4.2.4. *Boundary element model*

The physical and fictitious boundaries of the RVE are discretized into 41033 eight-noded quadratic quadrilateral and six-noded quadratic triangular elements, as shown in Fig. 8(a) and 8(b). Note that the discretizations on the fictitious surfaces S_{f_1} and S_{f_2} must be identical to apply the periodic boundary conditions (9) and (10) at the nodes of the elements.

4.2.5. *Numerical results of the macrocell corrosion*

In this section, the numerical results for the macrocell corrosion problem are presented. The computed potential and current density distributions at the surface of the rebar frame are presented in Figs. 9–11. More specifically, Fig. 9(a) and 9(b) depict the distributions at the entire rebar frame, while Figs. 10 and 11 illustrate the

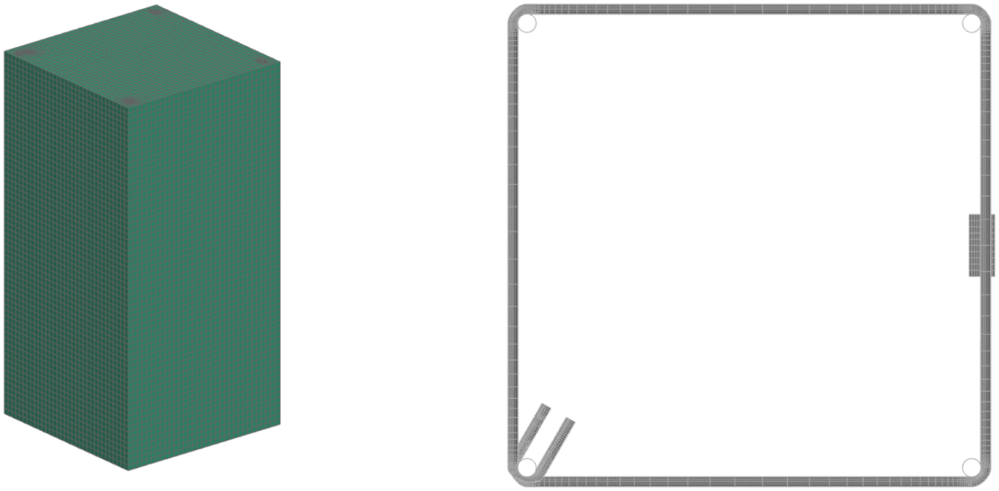

(a)

(b)

Fig. 8. Boundary element discretization: a) Concrete column, b) Rebar and anodes.

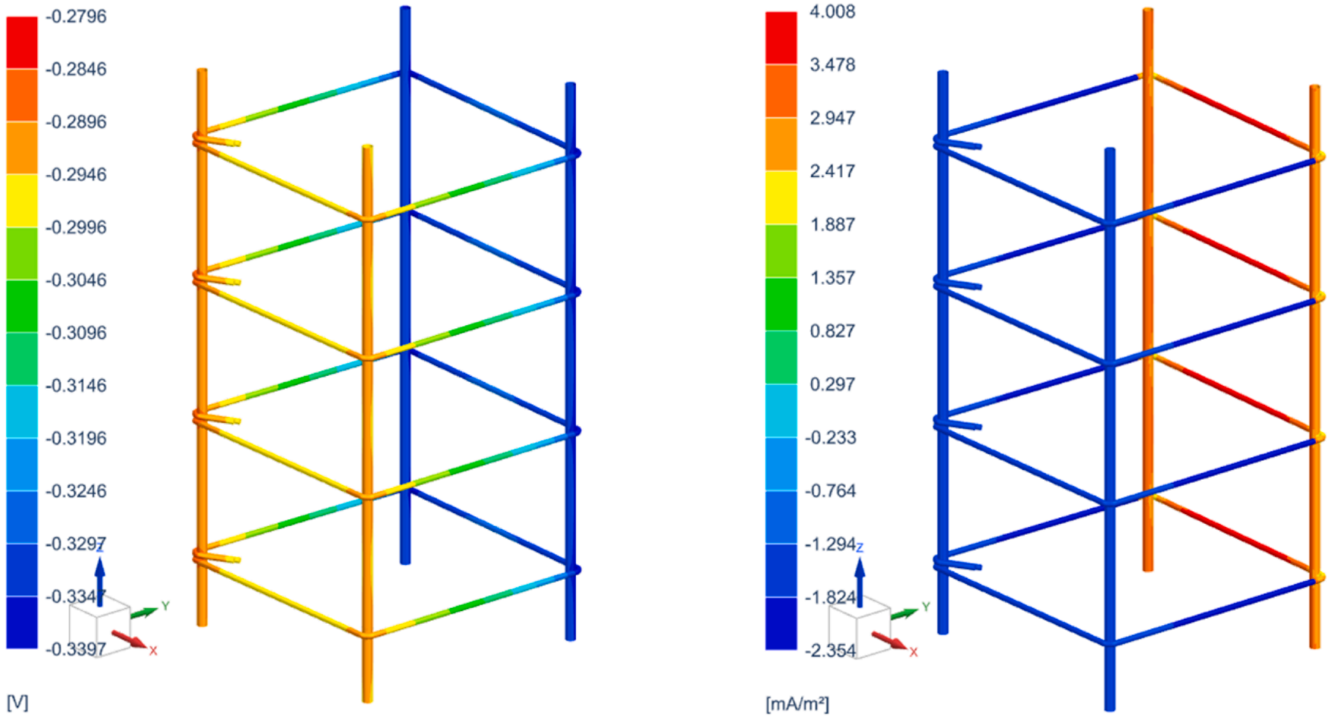

(a)

(b)

Fig. 9. Contour plot of (a) potential φ (V vs SCE) and (b) current density i (mA/m^2) at the entire rebar frame surface.

distributions at the active and passive surfaces, respectively.

Fig. 9 demonstrate that macrocell corrosion occurs at the rebar since the active and passive surfaces are anodic and cathodic, respectively. At the active rebar (Fig. 10), the maximum potential and current density are observed in the middle of the horizontal bars, while the minimum values appear at the connections between each horizontal bar with the vertical ones. In contrast, at the passive rebar (Fig. 11), the minimum potential and current density are observed at the active–passive interface, while the maximum values appear at the connection of the vertical bar with the start/end edges of each horizontal bar, as indicated in Fig. 11(a) with a circle.

4.2.6. *Numerical results of the cathodically protected steel rebar*

In this section, the numerical results for the cathodically protected steel rebar of the concrete column are presented. The computed potential and current density distributions at the surface of the rebar frame are shown in Figs. 12–14. More specifically, Fig. 12 depict the distributions at the entire rebar frame, while Figs. 13 and 14 illustrate the distributions at the active and passive surfaces of the rebar, respectively.

From Fig. 12, one can observe that both active and passive steel surfaces are cathodic due to the presence of the zinc anodes. At the active steel (Fig. 13), the maximum and minimum potential values are -0.453 and $-$ 0.650 V vs SCE, while the corresponding current density values are -10.42 and -51.99 mA/m^2. Furthermore, at the passive steel (Fig. 14), maximum and minimum potential values of -0.404 and

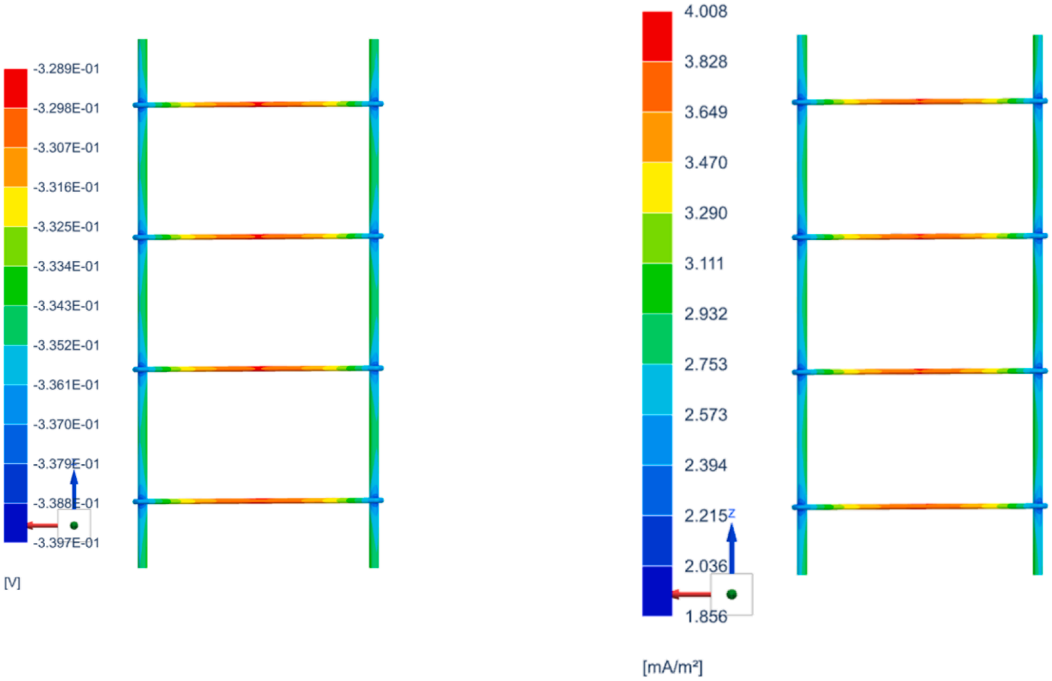

(a) (b)

Fig. 10. Contour plot of (a) potential φ (V vs SCE) and (b) current density i (mA/m^2) at the active rebar frame surface.

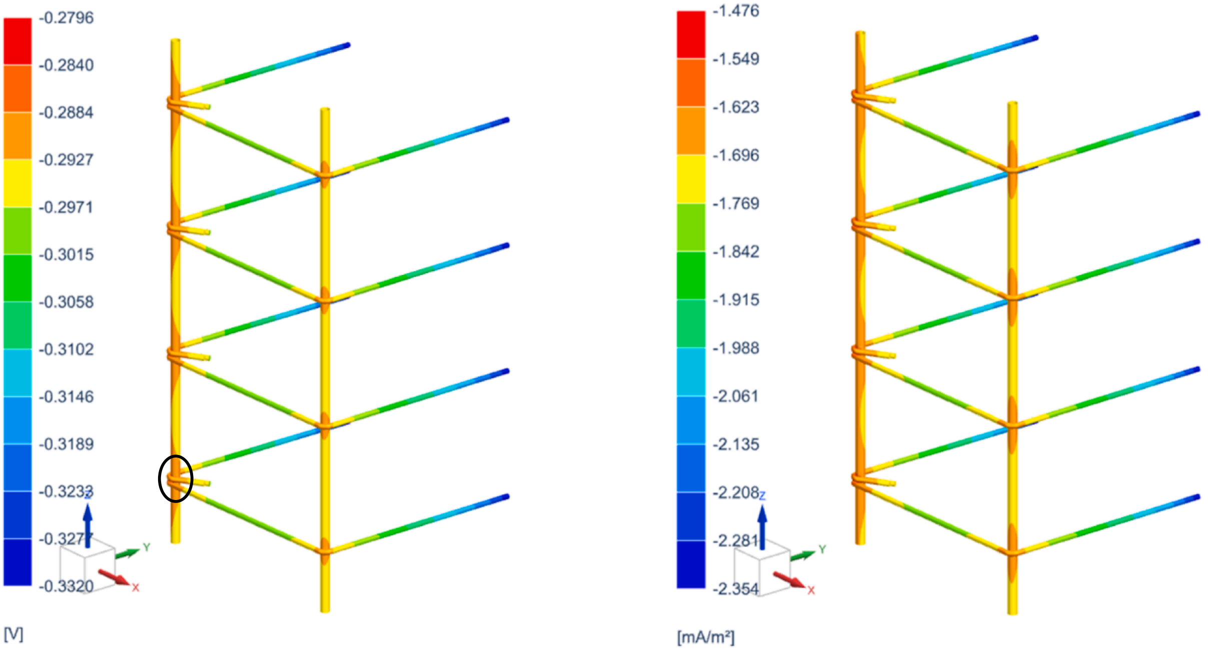

(a) (b)

Fig. 11. Contour plot of (a) potential φ (V vs SCE) and (b) current density i (mA/m^2) at the passive rebar frame surface.

-0.529 V vs SCE and corresponding current density values of -4.58 and -12.81 mA/m^2 are observed. In addition, from Fig. 12(b), 13(b) and 14 (b), one can observe a significant reduction of 39.18 mA/m^2 in the current density, flowing from the active to the passive steel. This reduction can be attributed to the lower overall reaction rate of passive steel.

Furthermore, the above results reveal that the protection criterion introduced by ISO [17] is fulfilled for the active rebar. Indeed, the minimum in magnitude cathodic current density is 10.42 mA/m^2, which is within the indicated ISO range of 2–20 mA/m^2. On the contrary, at the passive rebar, the cathodic current density minimum and maximum values (4.58 and 12.81 mA/m^2 in magnitude) are higher than the indicated ISO maximum value of 2 mA/m^2. Generally, higher current density values than the maximum proposed by ISO may cause active corrosion of the steel. However, examining this possibility is out of the scope of the present work.

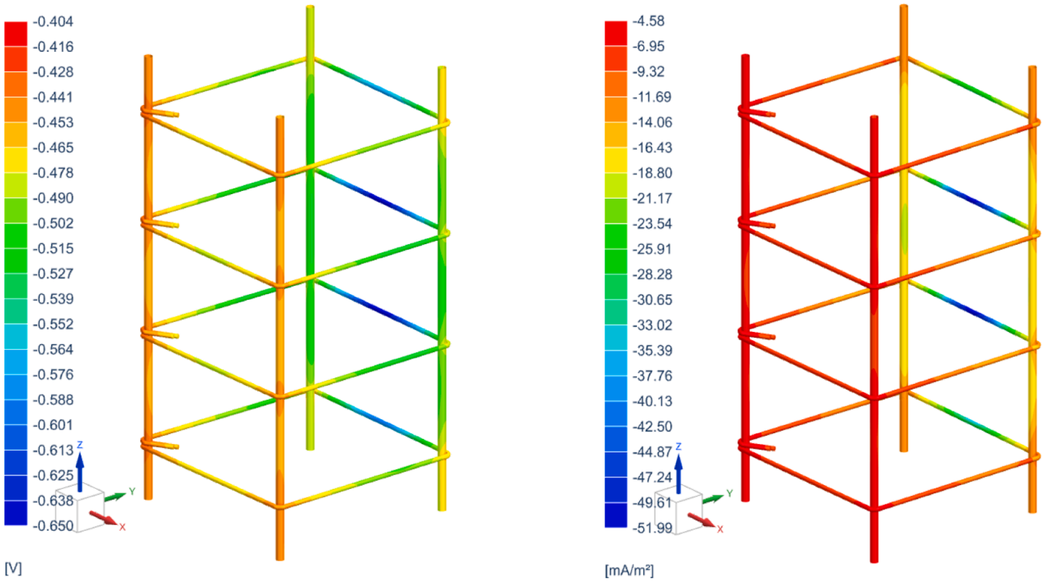

(a) (b)

Fig. 12. Contour plot of (a) potential φ (mV vs SCE) and (b) current density i (mA/m^2) at the entire rebar frame surface.

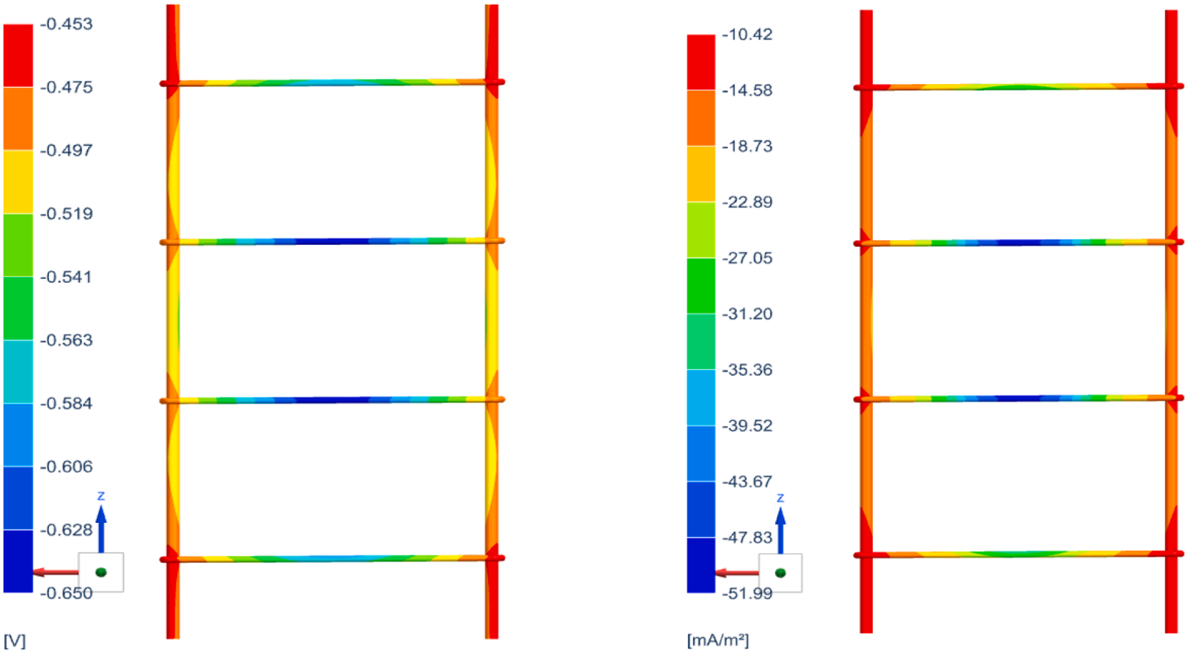

(a) (b)

Fig. 13. Contour plot of (a) potential φ (mV vs SCE) and (b) current density i (mA/m^2) at the active rebar frame surface.

Applying the CP system, the initial potential distribution due to the macrocell corrosion of Fig. 9(a) has changed to the one of Fig. 12(a), where the active steel surface has changed from anodic to cathodic. In Fig. 15(a) and 15(b), the contour plots of the cathodic polarization due to the application of the CP system at the active and passive rebar frame surfaces are presented, respectively.

From Fig. 15(a), a cathodic polarization of 115 mV is observed at the most anodic site. Thus, the introduced criterion by NACE [16] for at least a 100 mV cathodic polarization is also satisfied. Fig. 15(b) reveals a cathodic polarization of 124.2 mV at the less polarized site of the passive steel surface.

Consequently, according to both ISO and NACE protection criteria, the CP system provides sufficient protection.

Finally, in Fig. 16, the potential and current density distributions are presented at the connection between the start/end edges of the horizontal bars with the vertical bar, where the maximum values have been computed. This observation outlines the importance of detailed geometric modelling in such problems to ensure the efficiency of the CP system.

4.2.7. Performance of the SACP system to concrete conductivity

The performance of the CP system is significantly affected by the concrete conductivity σ [69]. Although σ typically ranges from 0.0005 to 0.02 S/m [60], the above analyses have been performed, adopting a

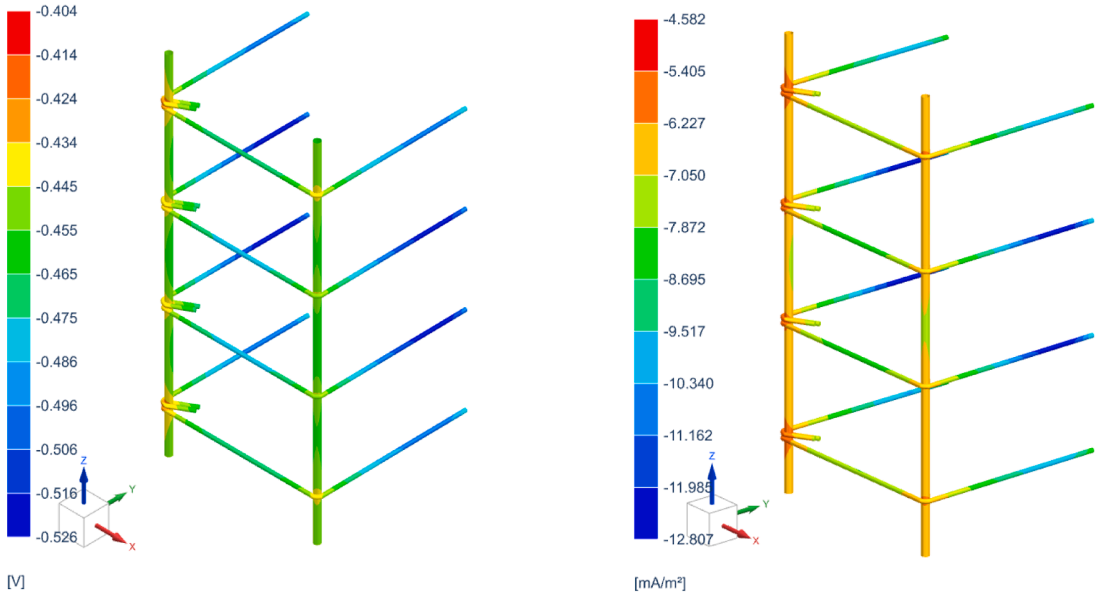

(a) (b)

Fig. 14. Contour plot of (a) potential φ (mV vs SCE) and (b) current density i (mA/m^2) at the passive rebar frame surface.

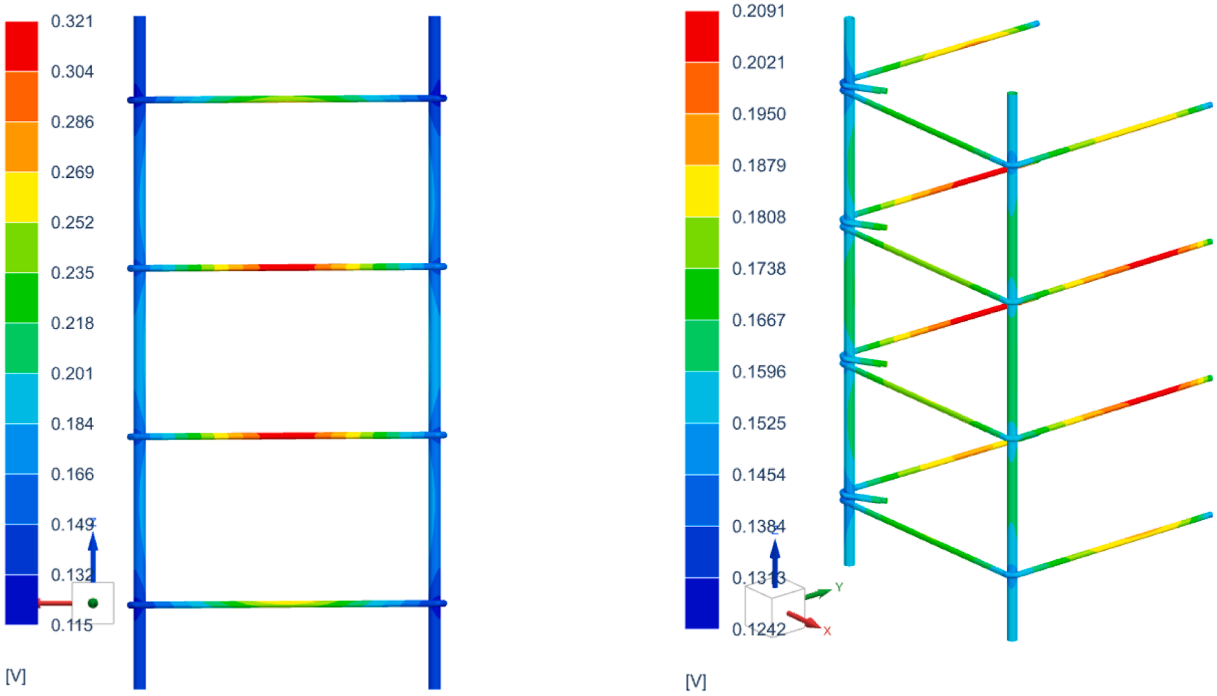

(a) (b)

Fig. 15. Contour plot of cathodic polarization due to the application of the CP system at the: (a) active and (b) passive rebar.

concrete conductivity of $\sigma = 0.01$ S/m.

In this section, a parametric study is carried out where the concrete conductivity takes values in the above range to evaluate the performance of the applied SACP system. To this end, the anode current output is calculated, and the fulfilment of ISO and NACE protection criteria is examined.

In Fig. 17, the anode current output I as a function of the concrete conductivity σ is shown. As the conductivity increases, the anode current output increases, and as expected, the CP system becomes more efficient.

In Fig. 18, the maximum current density i_{max} calculated at the active and passive steel surfaces is depicted as a function of the concrete conductivity σ. In agreement with the anode performance, the CP system is more efficient as the conductivity increases since the maximum current density monotonically increases. For $\sigma < 0.0015$ S/m, the delivered current density by the zinc anodes is insufficient to polarize the entire active steel surface to become cathodic since anodic sites due to macrocell corrosion are still observed. Furthermore, for the active rebar, the protection criterion introduced by ISO [17] is fulfilled for $\sigma > 0.003$ S/m, as the minimum in magnitude cathodic current density is greater

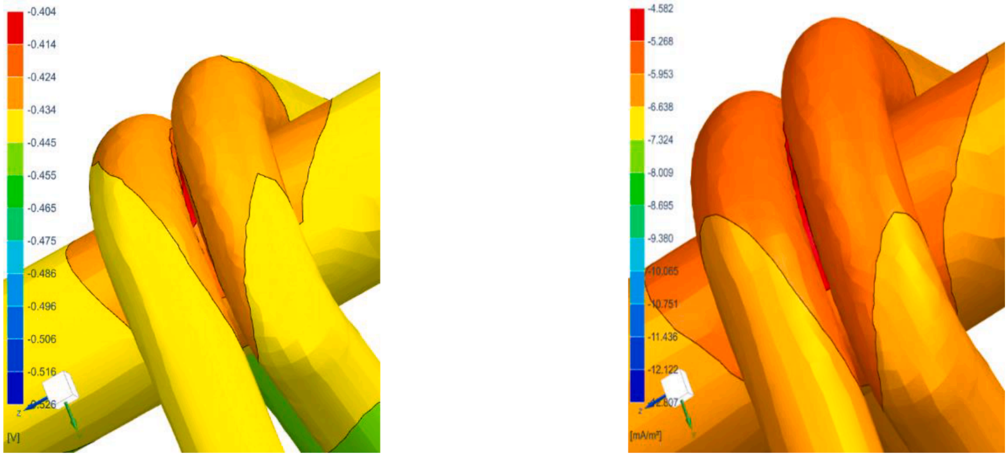

(a) (b)

Fig. 16. Contour plot detail of (a) potential φ (mV vs SCE) and (b) current density i (mA/m^2) at the passive rebar frame surface.

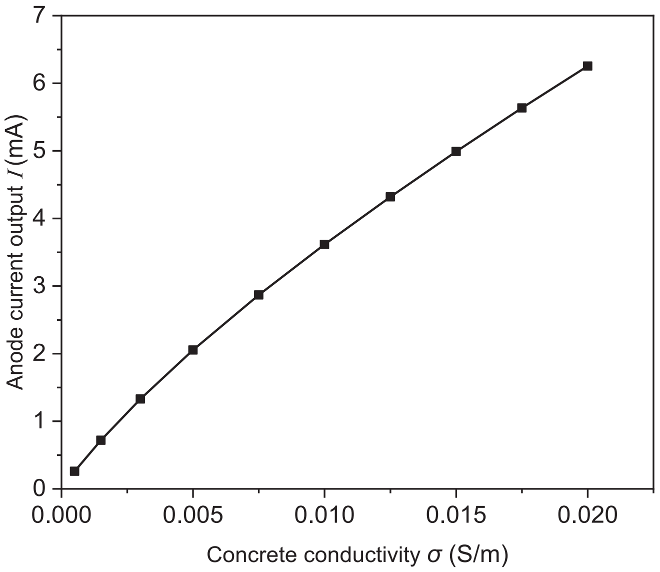

Fig. 17. Anode current output I as a function of the concrete conductivity σ.

than the indicated by ISO minimum value of 2 mA/m^2. Regarding the passive rebar, the ISO criterion is fulfilled for all examined conductivity values since all the calculated minimum in magnitude cathodic current densities are greater than the indicated ISO minimum value of 0.2 mA/m^2.

Fig. 19(a) depicts the maximum and minimum potential φ at the active and passive steel surfaces as a function of conductivity σ. Similarly, the higher values of σ, the more cathodic polarization is observed. Fig. 19(b) shows the minimum cathodic polarization $\Delta\varphi_{\min}$ calculated in the active steel achieved by installing the CP system. For $\sigma > 0.0075$ S/m, the protection criterion introduced by NACE [16] is fulfilled since $\Delta\varphi_{\min}$ is greater than the indicated by NACE minimum value of 100 mV.

In conclusion, for low values of concrete conductivities, the SACP system, as expected, is not efficient. In addition, for the fulfilment of the ISO and NACE protection criteria, different lower limits of conductivity are found for the used CP system. More specifically, according to ISO, the minimum conductivity where the system is effective is 0.003 S/m, while according to NACE the corresponding value is 2.5 times higher, i.e. 0.0075 S/m.

5. Conclusion

An ACA/BEM formulation was proposed in the present work to treat CP problems exhibiting periodicity for the first time. The accuracy of the proposed formulation has been verified via the solution of a benchmark problem. Using the proposed method, the CP system of a reinforced

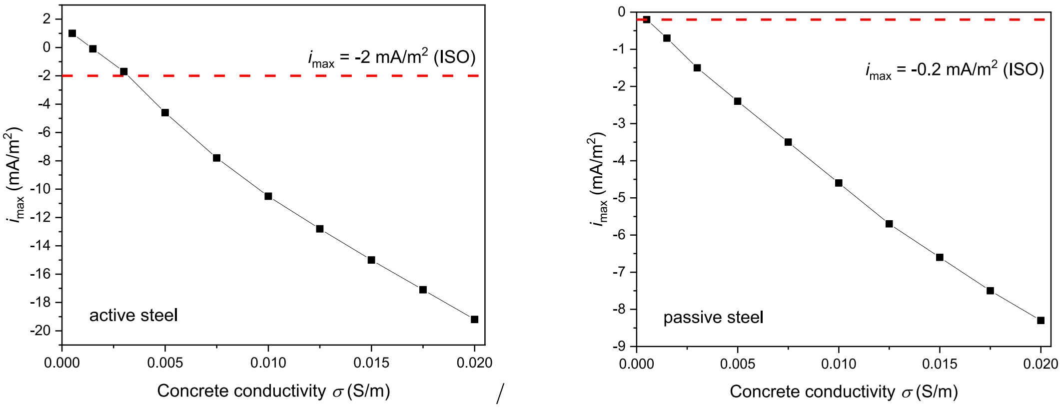

(a) (b)

Fig. 18. Maximum current density $i_{\max}$ at a) active and b) passive steel as a function of the concrete conductivity σ.

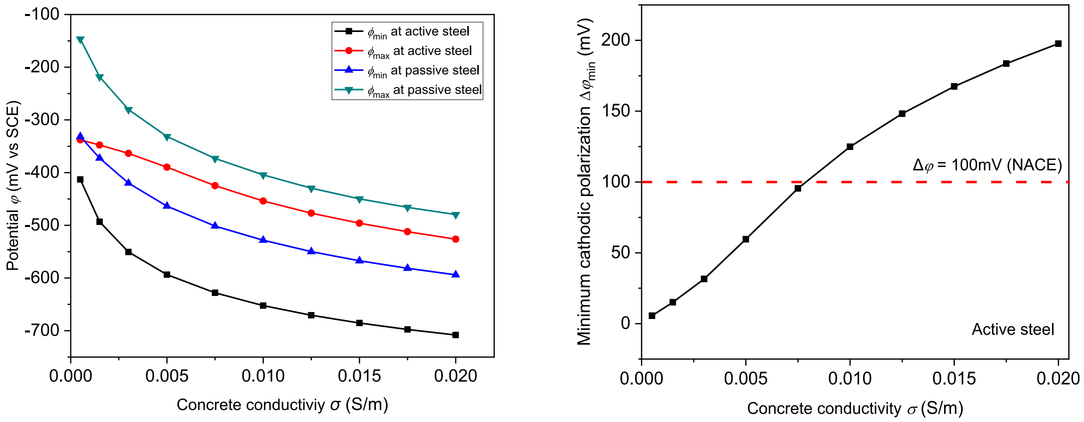

(a) (b)

Fig. 19. a) Maximum and minimum potential at active and passive steel b) minimum cathodic polarization at active steel versus concrete conductivity.

concrete column exhibiting both active and passive behavior due to carbonation and chloride contamination has been analyzed. The performance of the CP system has been examined according to ISO and NACE corrosion protection criteria. To this end, the macrocell corrosion problem was initially solved, and a parametric study with respect to concrete conductivity was carried out.

CRediT authorship contribution statement

Dimitrios T. Kalovelonis: Software, Methodology, Visualization, Investigation, Writing – original draft. **Theodoros V. Gortsas:** Software, Methodology, Visualization, Writing – review & editing. **Stephanos V. Tsinopoulos:** Conceptualization, Methodology, Supervision, Writing – review & editing.

Declaration of Competing Interest

The authors declare that they have no known competing financial interests or personal relationships that could have appeared to influence the work reported in this paper.

Data availability

Data will be made available on request.

Acknowledgement

The authors are grateful to Mr N. Tsoulos, Civil Engineer, for providing us with the geometry of the analyzed reinforced concrete column and Mr K. Loukas, Project Engineer at FEAC Engineering, for the solution of the benchmark problem with Siemens Simcenter STAR-CCM+.

References

[1] B.N. Popov, Corrosion engineering principles and solved problems, Elsevier, Amsterdam, 2015.
[2] K. Tuutti, corrosion of steel in concrete, Swedish Cement and Concrete Institute, Stockholm, 1982.
[3] P. Arora, B.N. Popov, B. Haran, M. Ramasubramanian, S. Popova, R.E. White, Corrosion initiation time of steel reinforcement in a chloride environment-a one dimensional solution, Corr. Sci. 39 (4) (1997) 739–759.
[4] J. Warkus, M. Raupach, Numerical modelling of macrocells occurring during corrosion of steel in concrete, Mater. Corros. 59 (2) (2008) 122–130, https://doi.org/10.1002/maco.200804164.
[5] F. Bolzoni, M. Ormellese, M. Pedeferri, E. Proverbio, Big milestones in the study of steel corrosion in concrete, Struct. Concr. 24 (1) (2023) 115–126.
[6] G.K. Glass, N.R. Buenfeld, The influence of chloride binding on the chloride induced corrosion risk in reinforced concrete, Corros. Sci. 42 (2) (2000) 329–344.
[7] G.K. Glass, N.R. Buenfeld, Theoretical assessment of the steady state diffusion cell test, J. Mater. Sci. 33 (1998) 5111–5118.
[8] N.S. Berke, M.P. Dallaire, R.E. Weyers, M. Henry, J.E. Peterson, B. Prowell, Corrosion forms and control for infrastructure, in: V. Chaker (Ed.), ASTM STP 1137, ASTM International, Philadelphia, PA, 1992, pp. 300–327.
[9] Brenna, A., Diamanti, M. V., Lazzari, L., & Ormellese, M. (2011). A proposal of AC corrosion mechanism in cathodic protection. In Proceedings of the 2011 NSTI Nanotechnology Conference and Expo, Boston, MA, USA, 13–16 June 2011; pp. 553–556.
[10] A. Brenna, M. Ormellese, L. Lazzari, Electromechanical breakdown mechanism of passive film in alternating current-related corrosion of carbon steel under cathodic protection condition, Corrosion 72 (8) (2016) 1055–1063, https://doi.org/10.5006/1849.
[11] A. Brenna, S. Beretta, F. Bolzoni, M. Pedeferri, M. Ormellese, Effects of AC-interference on chloride-induced corrosion of reinforced concrete, Constr. Build. Mater. 137 (2017) 76–84, https://doi.org/10.1016/j.conbuildmat.2017.01.087.
[12] A. Brenna, S. Beretta, M. Ormellese, AC corrosion of carbon steel under cathodic protection condition: assessment, Criteria Mech. rev. Mater. 13 (9) (2020), https://doi.org/10.3390/ma13092158.
[13] F. Bolzoni, A. Brenna, M. Ormellese, Recent advances in the use of inhibitors to prevent chloride-induced corrosion in reinforced concrete, Cem. Concr. Res. 154 (2022), 106719, https://doi.org/10.1016/j.cemconres.2022.106719.
[14] The National Association of Corrosion Engineers, NACE standard SP0187-2017: design considerations for corrosion control of reinforcing steel in concrete, NACE International, Houston, 2017.
[15] A. James, E. Bazarchi, A.A. Chiniforush, P. Panjebashi Aghdam, M.R. Hosseini, A. Akbarnezhad, I. Martek, F. Ghodoosi, Rebar corrosion detection, protection, and rehabilitation of reinforced concrete structures in coastal environments: a review, Constr. Build. Mater. 224 (2019) 1026–1039, https://doi.org/10.1016/j.conbuildmat.2019.07.250.
[16] The National Association of Corrosion Engineers, NACE standard RP0290-2000: impressed current cathodic protection of reinforcing steel in atmospherically exposed concrete structures, NACE International, Houston, 2011.
[17] CENELEC - European Committee for Electrotechnical Standardization, 2016. Cathodic protection of steel in concrete. CENELEC, Brussels.
[18] P. Pedeferri, Cathodic protection and cathodic prevention, Constr. Build. Mater. 10 (5) (1996) 391–402.
[19] J.W. Fu, J.S.K. Chow, CATHODIC PROTECTION DESIGNS USING AN INTEGRAL-EQUATION NUMERICAL-METHOD, Mater. Perform. 21 (10) (1982) 9–12.
[20] Danson, D.J., and Warne, M.A.: Current density/voltage calculations using boundary element techniques, Proc. Corrosion/83, Paper No. 211, 1983.
[21] R.A. Adey, S.M. Niku, C.A. Brebbia, J. Finnegan, Computer aided design of cathodic protection systems, Appl. Ocean Res. 8 (4) (1986) 209–222, https://doi.org/10.1016/S0141-1187(86)80037-2.
[22] N. Zamani, Boundary element simulation of the cathodic protection system in a prototype ship, Appl. Math Comput. 26 (1988) 119–134, https://doi.org/10.1016/0096-3003(88)90046-X.
[23] S. Aoki, K. Kishimoto, Application of BEM to galvanic corrosion and cathodic protection, in: C.A. Brebbia (Ed.), Electrical Engineering Applications, Springer, Berlin Heidelberg, 1990, pp. 65–86, https://doi.org/10.1007/978-3-642-48837-5_4.
[24] J.C.F. Telles, W.J. Mansur, L.C. Wrobel, M.G. Marinho, Numerical simulation of a cathodically protected semisubmersible platform using the PROCAT system, Corrosion 46 (6) (1990) 513–518, https://doi.org/10.5006/1.3585141.
[25] D.C. Rodopoulos, T.V. Gortsas, S.V. Tsinopoulos, D. Polyzos, ACA/BEM for solving large-scale cathodic protection problems, Eng. Anal. Bound. Elem. 106 (2019) 139–148, https://doi.org/10.1016/j.enganabound.2019.05.011.
[26] D.T. Kalovelonis, D.C. Rodopoulos, T.V. Gortsas, S.V. Tsinopoulos, D. Polyzos, Cathodic protection of a container ship using a detailed BEM model, J. Mar. Sci. Eng. 8 (2020) 359–373, https://doi.org/10.3390/jmse8050359.

[27] T.V. Gortsas, S.V. Tsinopoulos, D. Polyzos, An accelerated boundary element method via cross approximation of integral kernels for large-scale cathodic protection problems, ComputAided Civ Inf. 37 (7) (2022) 848–863.

[28] M. Purcar, B. Van den Bossche, L. Bortels, J. Deconinck, P. Wesselius, Numerical 3-D simulation of a cathodic protection system for a buried pipe segment surrounded by a load relieving U-shaped vault, Corrosion 59 (2003) 1019–1028, https://doi.org/10.5006/1.3277520.

[29] D.P. Riemer, M.E. Orazem, A mathematical model for the cathodic protection of tank bottoms, Corros. Sci. 47 (3) (2005) 849–868, https://doi.org/10.1016/j.corsci.2004.07.018.

[30] S. Fonna, S. Huzni, A. Zaim, Simulation of cathodic protection on reinforced concrete using BEM, JMechE 4 (2) (2017) 111–122.

[31] M. Masuda, M. Arita, L.E. Ju, K. Hanada, H. Minagawa, K. Kawamata, The application of FEM to cathodic corrosion protection of steel reinforcement in concrete, Mater. Trans. 45 (12) (2004) 3349–3355, https://doi.org/10.2320/matertrans.45.3349.

[32] J. Warkus, M. Brem, M. Raupach, BEM-models for the propagation period of chloride induced reinforcement corrosion, Mater. Corros. 57 (8) (2006) 636–641, https://doi.org/10.1002/maco.200603995.

[33] J. Gulikers, M. Raupach, Numerical models for the propagation period of reinforcement corrosion - comparison of a case study calculated by different researchers, Mater. Corros. 57 (8) (2006) 618–627, https://doi.org/10.1002/maco.200603993.

[34] Brem, M. (2004), Numerische Modellierung der Korrosion in Stahlbetonbauten: Anwendung der Boundary Element Methode, Eidgenössischen Technischen Hochschule Zürich.

[35] J. Warkus, M. Raupach, Modelling of reinforcement corrosion – geometrical effects on macrocell corrosion, Mater. Corros. 61 (6) (2010) 494–504, https://doi.org/10.1002/maco.200905437.

[36] J. Warkus, M. Raupach, Modelling of reinforcement corrosion – Corrosion with extensive cathodes, Mater. Corros. 57 (12) (2006) 920–925, https://doi.org/10.1002/maco.200604032.

[37] F. Brichau, J. Deconinck, T. Driesens, Modeling of underground cathodic protection stray currents, Corrosion 52 (6) (1996) 480–488.

[38] J. Trevelyan, H.P. Hack, Analysis of stray current corrosion problems using boundary method, in: C.A. Brebbia (Ed.), WIT Transactions on Modelling and Simulation, vol 8, WIT Press, Southampton, 1994, pp. 347–356.

[39] R.A. Adey, J. Baynham, Computer simulation as an aid to CP system design and interference prediction, in Proc. Of the CEOCOR 2000 Conference, 2000.

[40] D.T. Kalovelonis, T.V. Gortsas, S.V. Tsinopoulos, D. Polyzos, Accelerated boundary element method for direct current interference of cathodic protections systems, Ocean Eng. 258 (2022) 111705.

[41] J. Deconinck, G. Maggetto, J. Vereecken, Calculation of current distribution and electrode shape change by the boundary element method, J. Electrochem. Soc. 132 (12) (1985) 2960–2965, https://doi.org/10.1149/1.2113701.

[42] V.G. DeGiorgi, Evaluation of perfect paint assumptions in modeling of cathodic protection systems, Eng. Anal. Bound. Elem. 26 (5) (2002) 435–445, https://doi.org/10.1016/S0955-7997(01)00104-7.

[43] F. Brichau, J. Deconinck, A numerical model for cathodic protection of buried pipes, Corrosion 50 (1) (1994) 39–49, https://doi.org/10.5006/1.3293492.

[44] Riemer, D.P., Orazem, M.E., 2005. Modeling coating flaws with non-linear polarization curves for long pipelines, in: Brebbia, C. A. (Ed.), WIT Transactions on State of the Art in Science and Engineering vol 7, WIT Press, Southampton, pp. 225-257. https://doi.org/10.2495/1-85312-889-9/09.

[45] S. Aoki, K. Amaya, Optimization of cathodic protection system by BEM, Eng. Anal. Bound. Elem. 19 (2) (1997) 147–156, https://doi.org/10.1016/S0955-7997(97)00019-2.

[46] N.G. Zamani, J.M. Chuang, Optimal control of current in a cathodic protection system: a numerical investigation, Optimal Control Appl. Methods 8 (4) (1987) 339–350, https://doi.org/10.1002/oca.4660080404.

[47] P. Miltiadou, L.C. Wrobel, A BEM-based genetic algorithm for identification of polarization curves in cathodic protection systems, Int. J. Numer. Meth. Eng. 54 (2) (2002) 159–174, https://doi.org/10.1002/nme.413.

[48] E. Santana Diaz, R. Adey, Optimising the location of anodes in cathodic protection systems to smooth potential distribution, Adv. Eng. Softw. 36 (9) (2005) 591–598.

[49] Kalovelonis, D. T., Gortsas, T. V., Tsinopoulos, S. V., & Polyzos, D. (2022). Optimal Design of a Sacrificial Anode Cathodic Protection System for an Offshore Wind Turbine Jacket Foundation via Accelerated BEM, No 44, 13th congress of Hellenic Society of Theoretical and applied mechanics, Stavroulakis, G.E., Polyzos, D., & Hatzigeorgiou, G.D. (ed.), Patras, Greece. ISSN/E-ISSN: /2944-9359, ISBN/978-960-530-181-1.

[50] M. Ihsan, S. Fonna, R. Kurniawan, Z. Fuadi, A.K. Ariffin, Computational modelling for RC cylindrical column corrosion using axisymmetric BEM, IEEE Int. Conf. Cybernetics Computational Intelligence (CyberneticsCom) 2019 (2019) 82–86, https://doi.org/10.1109/CYBERNETICSCOM.2019.8875678.

[51] L.Q. Liu, H.T. Wang, A line model-based fast boundary element method for the cathodic protection analysis of pipelines in layered soils, CMES 90 (6) (2013) 439–462.

[52] Keddie, A.J., Pocock, M.D., DeGiorgi, V.G., 2007. Fast solution techniques for corrosion and signatures modelling, in: Brebbia, C. A. (Ed.), WIT Transactions on Engineering Sciences vol 54, WIT Press, Southampton, pp. 225-234. https://doi.org/10.2495/ECOR070221.

[53] Y.J. Liu, Fast multipole boundary element method: theory and applications in engineering, Cambridge University Press, 2009.

[54] M.M.S. Cheung, C. Cao, Application of cathodic protection for controlling macrocell corrosion in chloride contaminated RC structures, Constr. Build. Mater. 45 (2013) 199–207, https://doi.org/10.1016/j.conbuildmat.2013.04.010.

[55] A. Goyal, E.K. Olorunnipa, H.S. Pouya, E. Ganjian, A.O. Olubanwo, Potential and current distribution across different layers of reinforcement in reinforced concrete cathodic protection system- A numerical study, Constr. Build. Mater. 262 (2020), 120580, https://doi.org/10.1016/j.conbuildmat.2020.120580.

[56] Siemens Digital Industries Software. Simcenter STAR-CCM+, version 2022.1, Siemens 2022.

[57] J. Newman, K.E. Thomas-Alyea, Electrochemical systems, third ed., John Wiley & Sons, New Jersey, 2004.

[58] J.C.F. Telles, W.J. Mansur, L.C. Wrobel, On boundary elements for external potential problems, Mech. Res. Commun. 11 (6) (1984) 373–377, https://doi.org/10.1016/0093-6413(84)90044-2.

[59] D. Polyzos, S.V. Tsinopoulos, D.E. Beskos, Static and dynamic boundary element analysis in incompressible linear elasticity, Eur. J. Mech. A Solids 17 (3) (1998) 515–536.

[60] K. Hornbostel, C.K. Larsen, M.R. Geiker, Relationship between concrete resistivity and corrosion rate – a literature review, Cem. Concr. Compos. 39 (2013) 60–72, https://doi.org/10.1016/j.cemconcomp.2013.03.019.

[61] J. Ge, O.B. Isgor, Effects of Tafel slope, exchange current density and electrode potential on the corrosion of steel in concrete, Mater. Corros. 58 (8) (2007) 573–582, https://doi.org/10.1002/maco.200604043.

[62] S.C. Kranc, A.A. Sagüés, Detailed modeling of corrosion macrocells on steel reinforcing in concrete, Corros. Sci. 43 (7) (2001) 1355–1372, https://doi.org/10.1016/S0010-938X(00)00158-X.

[63] J. Gulikers, Theoretical considerations on the supposed linear relationship between concrete resistivity and corrosion rate of steel reinforcement, Mater. Corros. 56 (6) (2005) 393–403, https://doi.org/10.1002/maco.200403841.

[64] F. Wang, J. Xu, Y. Xu, L. Jiang, G. Ma, A comparative investigation on cathodic protections of three sacrificial anodes on chloride-contaminated reinforced concrete, Constr. Build. Mater. 246 (2020), 118476, https://doi.org/10.1016/j.conbuildmat.2020.118476.

[65] T.P. Hills, F. Gordon, N.H. Florin, P.S. Fennell, Statistical analysis of the carbonation rate of concrete, Com. Con. Res. 72 (2015) 98–107, https://doi.org/10.1016/j.cemconres.2015.02.007.

[66] S. Zhang, Experimental data treatment of the pipeline steel polarization curve under AC interference, Int. J. Electrochem. Sci. (2019) 10888–10906, https://doi.org/10.20964/2019.12.05.

[67] A.M. Hassanein, G.K. Glass, N.R. Buenfeld, Protection current distribution in reinforced concrete cathodic protection systems, Cem. Concr. Compos. 24 (1) (2002) 159–167, https://doi.org/10.1016/S0958-9465(01)00036-1.

[68] O.B. Isgor, A.G. Razaqpur, Modelling steel corrosion in concrete structures, Mater. Struct. 39 (3) (2006) 291–302, https://doi.org/10.1007/s11527-005-9022-7.

[69] C. Helm, M. Raupach, Numerical evaluation of the capacity of galvanic anode systems for patch repair of reinforced concrete structures, Mater. Corros. 71 (5) (2020) 726–737, https://doi.org/10.1002/maco.202011578.